nature communications

Article

https://doi.org/10.1038/s41467-025-63540-w

Ten thousand hour stable zinc air batteries via Fe and W dual atom sites

Received: 9 January 2025

Accepted: 22 August 2025

Published online: 29 August 2025

Check for updates

Yifan Li[1], Hanlin Wang[1], Chang Chen[2], Xuesong Xie[1], Yang Yang[1], Xuehai Tan[1], Keren Jiang[1], Ning Chen[3], Hao Zhang[1] ✉ & Zhi Li[1] ✉

Durable and highly active oxygen electrocatalysts are crucial to the large-scale application of rechargeable zinc-air batteries. Here we utilize the N_4 unit in phthalocyanine molecule to trap the tungsten atoms scratched off from the tungsten carbide milling balls and place the obtained W-N_4 unit adjacent to the Fe-N_4 units from iron (II) phthalocyanine, resulting in highly active Fe-N_4/W-N_4 diatomic sites with well-pronounced 3*d*–5*d* hybrid for efficient and durable oxygen electrocatalysis. The electron distribution of the Fe-N_4 site is optimized by the neighboring W-N_4 site, which facilitates the O_2 activation and the desorption of *OH and enhances the catalytic activity of the Fe-N_4 site. Meanwhile, the unsaturated 5 *d* orbitals and tunable valence of the W atoms could modulate the electronic state of the Fe species, prevent leaching, and further enhance the catalytic stability. The resulting zinc-air battery with Fe,W-N-C air cathode exhibits notable cycling stability and repeatability for over 10,000 h. This enhanced stability highlights the possibility of developing 5 *d* metal-boosted 3 *d* metal active sites for the fabrication of efficient oxygen electrocatalysts and stable zinc-air batteries.

The oxygen reduction reaction (ORR) is an important cathodic reaction in emerging energy technologies such as metal-air batteries and fuel cells, which involves multi-electron and proton-coupling processes[1,2]. Its sluggish kinetics and the high cost of commercial Pt-based electrocatalysts severely limit the widespread commercial applications[3,4]. Among the atomically dispersed metal catalysts, the Fe-N_4 sites with a porphyrin-like structure are widely recognized as one of the most promising sites for ORR[5–8]. However, the symmetric electron distribution of the Fe-N_4 site and the limited orbital overlap between Fe 3 *d* and O 2*p* orbitals increase the energy requirements to activate the O_2 ($*O_2 \rightarrow *OOH$)[9–11]. The strong affinity of OH^- on the Fe-N_4 sites hinders the desorption of *OH, resulting in large overpotentials due to the accumulation of OH^-[12–17]. Moreover, at high potentials, the FeNC/Fe^{2+} thermodynamic equilibrium will shift toward the formation of Fe^{2+}, and the leaching and dissolution of the Fe sites during the ORR process will cause decrements of the catalytic stability and further limit the commercial applications of the Fe-based catalysts[18–20].

Inspired by the Cu-Fe bimetallic atomic structure of cytochrome *c* oxidase, a natural oxidoreductase often found in animals and plants, researchers realized that they might need another atom with different radii and electronegativities forming bimetallic configuration with Fe to break the electronic density plane symmetry of the Fe-N_4 sites[21]. The interaction between two different atoms may mitigate the dissolution of the Fe center and enhance the catalytic stability[22]. Recently, numerous efforts have been devoted to designing dual-atom catalysts with bimetallic active sites, such as Fe-Co, Fe-Cu, and Fe-Ni[23–26]. Although these diatomic catalysts exhibit improved ORR catalytic activity relative to single-atom catalysts due to the synergistic effect of the bimetallic sites, the electronic structure of these second metals (3 *d*) is quite close to Fe, making them less efficient in breaking the symmetrical charge distribution[27]. Therefore, introducing metal atoms that cause more asymmetric electron distribution seems to be a straightforward solution. Wang et al. found that the Ir possesses increased 5 *d* electronic wave function spatial extent, and can

[1]Department of Chemical and Materials Engineering, University of Alberta, Edmonton, AB, Canada. [2]Engineering Research Center of Advanced Rare Earth Materials, Department of Chemistry, Tsinghua University, Beijing, China. [3]Hard X-Ray Micro Analysis BL, Canadian Light Source Saskatoon, Saskatoon, SK, Canada. ✉e-mail: hao.zhang@ualberta.ca; zhi.li@ualberta.ca

effectively modulate the electronic structure and local coordination environment of 3 *d* transition metals Ni-Fe oxyhydroxides[28], because of the stronger hybridization with neighboring ligand orbitals[29]. In addition, 5 *d* metals have additional orbital degrees of freedom to tailor the electronic band structure and the adsorption and desorption energy of the intermediates[30]. Xin et al. also utilized the difference in electronegativity between the two metals in a diatomic catalyst to optimize the electron distribution at the active site[31]. Therefore, it is reasonable to speculate that if a 5 *d* metal with large radii, multiple valence states, and different electronegativity can be introduced as the second metal near the Fe-N_4 site to form a Fe-5*d* M diatomic site, it will be more conducive to the occurrence of ORR. Among the 5 *d* transition metals, W is a promising candidate with demonstrated electrocatalytic activity in single-atom form, and the activity is sensitive to coordination number[32–34]. The challenge of using W as the second metal site lies in synthesizing such electrocatalysts with rationally designed 3*d*–5*d* diatomic sites using minimal resources and facile processes suitable for large-scale industrial applications. In fact, the identification of the hetero-diatomic structure itself is complicated enough. Aberration-corrected high-angle annular dark-field scanning transmission electron microscopy (HAADF-STEM) analysis often shows many diatomic couples, and EELS analysis is required to confirm the coexistence of two metals in a small zone (e.g., 1×1 nm). Unless a significant portion of diatomic couples is individually analyzed by EELS, which is often impractical, it is risky to conclude that the dominating structure is hetero-diatomic (A-B) or homo-diatomic (A-A or B-B). The 3*d*–5*d* diatomic sites can be judged more intuitively through the difference in brightness of the HAADF-STEM image, which could provide favorable support for the precise synthesis of diatomic catalysts.

Herein, we utilized the shear and impact forces during the high-energy ball milling to strip tungsten atoms from tungsten carbide milling balls and constructed a 3*d*–5*d* hybrid Fe,W-N-C catalyst with Fe-N_4/W-N_4 diatomic sites in carbon black support. The symmetrical charge distribution of the Fe-N_4 site is optimized by the neighboring W-N_4 site, and the Fe,W-N-C catalyst exhibits an ORR half-wave potential as high as 0.90 V and effectively four-electron ORR activity. Meanwhile, the mechanistic investigations reveal that the $*O_2$ activation energy and *OH desorption energy on Fe-N_4 sites could be significantly optimized by introducing the neighboring W-N_4 site. Importantly, the introduction of large radius 5*d*-W atoms adjacent to the Fe-N_4 site was found to be crucial to reduce the irreversible leaching of the Fe catalytic center and achieve unexpected oxygen catalytic stability. The zinc-air battery (ZAB) with Fe,W-N-C air cathode demonstrated a repeatable discharge/charge cycling stability for more than 10,000 h, which highlights its practical application potential.

Results

Synthesis of the 3*d*–5*d* hybrid Fe,W-N-C catalyst and structural characterization

High-energy ball milling has enough power to break and reform chemical bonds, often used to construct defects on the support, which could anchor isolated metal atoms/clusters, while the surface wearing of the milling balls is often overlooked[35]. Figure 1a illustrates the tungsten atoms falling off the tungsten carbide balls due to enormous shear and impact forces. When the raw material contains only carbon black, the fresh tungsten atoms with higher surface energy tend to combine with carbon atoms and aggregate into tungsten carbide nanoparticles during ball milling or subsequent pyrolysis steps (WC-C, Supplementary Figs. 1 and 2, Supplementary Table 1). In contrast, when sufficient phthalocyanine (Pc) complex is added, the tungsten atoms will stay isolated on the carbon black support (W-N-C, Supplementary Figs. 3 and 4). This could be attributed to the unique macrocyclic structure of Pc, with a central cavity occupied by two hydrogen atoms and surrounded by four nitrogen atoms in square planar geometry. This cavity is well-known for forming many stable metal complexes by replacing the two hydrogen atoms with metal atoms, such as Cu, Fe, Co, Ni, etc. When the two hydrogen atoms are knocked off during the ball milling process, the vacant cavity becomes an active trap for the fresh tungsten atoms, resulting in atomically dispersed W-N_4 sites.

Inspired by the successful construction of the W-N_4 site, we introduced one more component during the ball milling process: FePc, which possesses a similar structure to that of Pc but with two hydrogen atoms

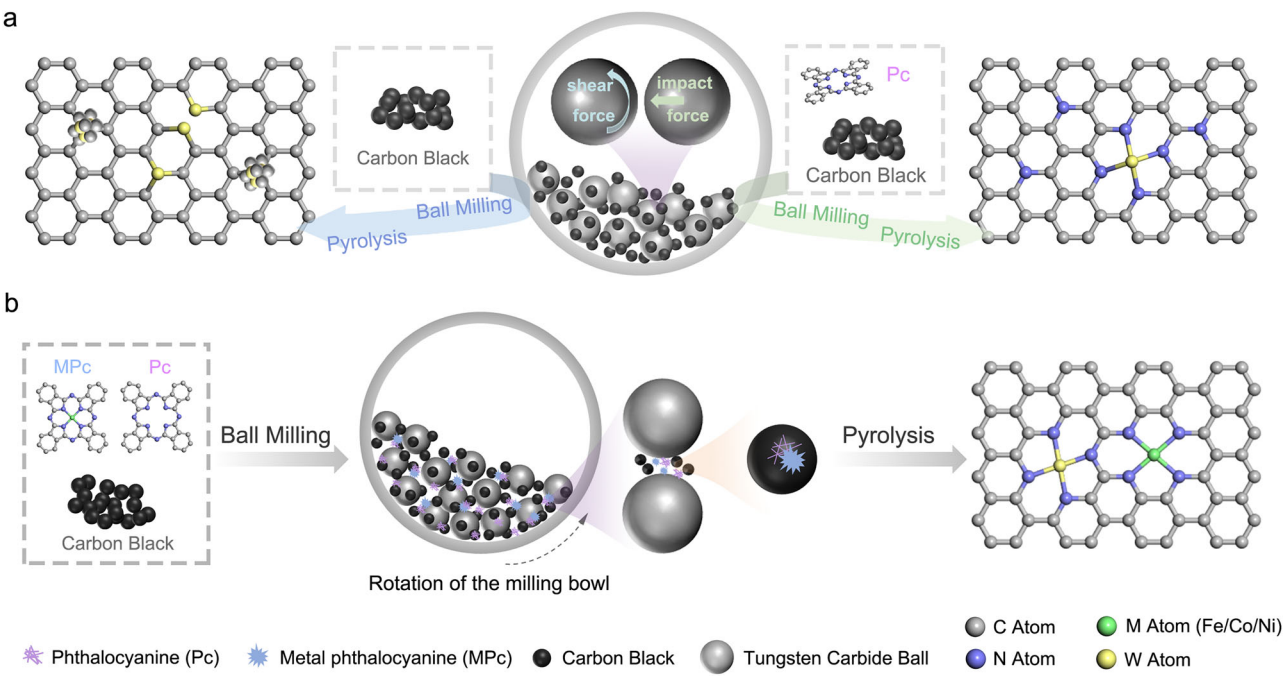

Fig. 1 | Schematic illustration of the synthesis procedure of different materials. **a** Tungsten carbide nanoparticles-carbon black catalyst (WC-C) and single-atom tungsten catalyst (W-N-C) obtained by stripping W atoms from tungsten carbide milling balls. **b** 3*d*-5*d* hybrid diatomic M,W-N-C catalysts (M = Fe/Co/Ni) obtained by co-introducing exogenous N-containing complex and 3 *d* metal-containing complex into the raw materials.

replaced by a Fe atom in the cavity, and constructed a 3*d*-5*d* Fe-W diatom catalytic site. As illustrated in Fig. 1b, in the highly energetic environment of ball milling (e.g., huge impact faces and high localized temperatures), the adsorption of both Pc and FePc molecules on the carbon black surface tends to reach thermodynamic equilibrium. Driven by the electron donor-acceptor interactions, the Pc and FePc tend to partially overlap and form N_4/FeN_4 on the carbon surface at equiblium[36,37]. When the N_4 portion of the N_4/FeN_4 site traps a highly active tungsten atom scratched off from the milling balls, the Fe-N_4/W-N_4 diatomic site is successfully constructed. After that, a pyrolysis process at 900 °C for 2 h in Ar atmosphere stabilizes the sites without sacrificing the coordinating N atoms or causing the aggregation of metal atoms[38–40]. It must be emphasized that 100% of the metals were utilized in the synthesis process. In the catalyst design, the Fe content is determined by the maximum amount of FePc allowed by atomic dispersion on carbon black, and the W content depends on the ball milling time to achieve the 1:1 atomic ratio. Extra milling time will introduce more W than that can be trapped and lead to the formation of tungsten carbide nanoparticles. Similarly, if the amount of Pc is insufficient, it will be difficult to introduce enough N_4 sites on the carbon black surface to fix the W atoms that fall off the ball mill, resulting in some W atoms forming WC nanoparticles (Supplementary Fig. 5). In the obtained catalysts, named Fe,W-N-C, the contents of Fe and W were optimized at 1.25 wt% and 4.02 wt% (the atom ratio of Fe and W is close to 1:1) as determined by inductively coupled plasma-optical emission spectroscopy (ICP-OES, Supplementary Table 1). To demonstrate the versatility of this catalyst construction strategy, we extended it to other representative 3*d*-metals (such as Co and Ni) by simply replacing FePc with other metal phthalocyanine complex and successfully synthesized Co,W-N-C and Ni,W-N-C 3*d*–5*d* hybrid dual-atom catalysts (Supplementary Figs. 6 and 7, Supplementary Table 1).

The dual-atom configuration of Fe,W-N-C catalyst was investigated using scanning electron microscopy (SEM) and transmission electron microscopy (TEM). As shown in Fig. 2a, b the Fe,W-N-C catalyst is composed of a series of pearl-like spherical carbon particles with diameters of 50-80 nm, and there are no obvious metal/ metal Pc nanoparticles in the carbon matrix. These results are consistent with the X-ray diffraction (XRD) patterns, in which only two broad diffraction peaks belonging to the (002) and (101) crystal planes of carbon were detected (Fig. 2c). The atomically dispersed Fe,W atom pairs were directly imaged by HAADF-STEM at the atomic scale. As shown in Fig. 2d, a large number of isolated bright-faint dot pairs are uniformly dispersed on the carbon black surface, marked by green rectangles. The pronounced brightness difference in each pair of atoms is due to the sensitive Z-contrast of heavy elements. Since only two metal elements are possible in the system, the pair can be safely identified as 3*d*-Fe (faint) and 5*d*-W (bright) atomic pair without guesswork. Supplementary Fig. 8 exhibits the corresponding intensity profile for two typical Fe-W bimetallic pairs at site 1 and site 2 in Fig. 2d, and it was found that the distance between the two metal atoms is about 0.55 nm, which is consistent with the distance in the atomic structure model of the 3*d*-5*d* hybridized Fe-N_4/W-N_4 diatomic site of the Fe,W-N-C catalyst pointed out in the density functional theory calculations part (Supplementary Fig. 9). In addition, the characteristic peaks of Fe and W atoms were both found in the electron energy loss spectroscopy (EELS) spectrum corresponding to the 1 nm × 1 nm small area HAADF-STEM image, providing another direct evidence of the existence of Fe and W diatomic sites (Fig. 2e–g)[41,42]. Since HAADF-STEM images describe two-dimensional projections, the projected distances between Fe and W atoms could differ (tagged by blue circles in Fig. 2d), depending on the angle between the W-Fe axis and the incident beam[43]. The lower magnification HAADF-STEM image and corresponding energy-dispersive X-ray spectroscopy (EDX) mapping also revealed the uniform distribution of C, N, W, and Fe elements in the Fe,W-N-C catalyst (Fig. 2h and Supplementary Fig. 10). High-resolution X-ray photoelectron spectroscopy (XPS) results confirmed the existence of sufficient N (from Pc and FePc molecules) in the Fe,W-N-C catalyst, which not only promoted the anchoring of Fe and W atoms on the carbon black surface but also generated graphitic nitrogen to improve electron transfer in the carbon skeleton (Supplementary Fig. 11)[44].

To gain more insight into the electronic structure and coordination environment of the 3*d*-Fe atom and 5*d*-W atom in Fe,W-N-C catalyst, X-ray absorption spectroscopy (XAS) was collected. As shown in Fig. 3a, a pre-edge peak at around 7114 eV was observed in the Fe K-edge X-ray absorption near edge structure (XANES), which is characteristic of the 1*s* to 4p_z electric dipole transition, along with the charge transfer from ligand to the metal center, and could be recognized as the fingerprint of the porphyrin-like planar Fe-N_4[45–48]. The absorption edge of the Fe,W-N-C catalyst is situated between FeO and Fe_2O_3, indicating that the oxidation state of Fe is between +2 and +3. To elucidate the effect of the neighboring 5*d*-W site on the chemical state of the Fe center, a single atom Fe-N-C catalyst without W was prepared as a reference through a similar procedure (Supplementary Figs. 12 and 13). Notably, the Fe K-edge absorption of the Fe,W-N-C catalyst is significantly lower than that of the Fe-N-C catalyst, implying that the introduction of 5*d*-W site neighboring to the 3*d*-Fe site can effectively regulate the oxidation state of the Fe atom, which could prevent the electrochemical dissolution of the Fe center and enhance its electrocatalytic stability (vide infra, Supplementary Fig. 14). The Fourier transformed k^3-weighted Fe K-edge extended X-ray absorption fine structure (EXAFS) spectrum of the Fe,W-N-C catalyst exhibited a prominent peak at around 1.5 Å, which could be assigned to the Fe-N contributions in the first shell (Fig. 3b). However, the main peak of the Fe-N-C catalyst is located at 1.41 Å (similar to the position shown in the FePc complex, Supplementary Fig. 15). The difference in peak position of Fe,W-N-C catalyst and Fe-N-C catalyst is due to the introduction of W-N_4 sites close to the Fe-N_4 sites in the Fe,W-N-C catalyst, which reduces the electron transfer from the Fe atoms to the surrounding environment, resulting in a decrease in the oxidation state of the Fe atoms and an increase in the Fe-N distance in Fe,W-N-C. Compared with Fe Foil, there is no observable Fe-Fe scattering peak at 2.2 Å in both of the Fe,W-N-C and Fe-N-C catalysts. This confirms the absence of Fe aggregates and verifies that Fe atoms exist in an atomically dispersed form. Due to the high resolution in *R*-space and *k*-space, the wavelet transform (WT)-EXAFS analysis was carried out to further reveal the isolated state of the Fe atoms. The Fe,W-N-C catalyst demonstrated an intensity maximum at k ~ 4.7 Å responding to the Fe-N bonds, and no metallic Fe-Fe scattering signal can be detected (Fig. 3c, and Supplementary Fig. 16). As shown in Fig. 3d–f and Supplementary Fig. 17, the W atoms also exhibited an atomically dispersed nature with an oxidation state between 0 and +6.

To clearly elucidate the coordination configurations of Fe and W atoms in the Fe,W-N-C catalyst, EXAFS fitting curves were simulated. As displayed in Fig. 3b, e and Supplementary Table 2, the fitting results indicated that both Fe and W atoms are coordinated with four N atoms in the first shell, with bond lengths of 1.90 Å and 2.09 Å, respectively. Since weak peaks at above 2.0 Å are observed in both the Fe K-edge EXAFS and W L_3-edge EXAFS spectra, combined with the weak WT-EXAFS intensity maximum in the k range of 5–7 $Å^{-1}$, which is higher than that of the coordination with C and different from the Fe-Fe or W-W peak, suggesting that a nonnegligible long-range interaction between the Fe and W atoms may occurred (Fig. 3b, c, e, f and Supplementary Fig. 17)[23,49]. We included the outer shells of Fe and W in EXAFS fitting. Although the distance between Fe and W is too long (about 5.5 Å revealed by HAADF-STEM) to be accurately fitted in EXAFS, the simulated spectra fitted to the 4^{th} shell of Fe (R = 3.33 Å) and the 5^{th} shell of W (R = 4.29 Å) overlapped well in the experimental spectra, which further proved that the atomic structure model of the 3*d*–5*d* hybridized Fe-N_4/W-N_4 diatomic site of the Fe,W-N-C catalyst

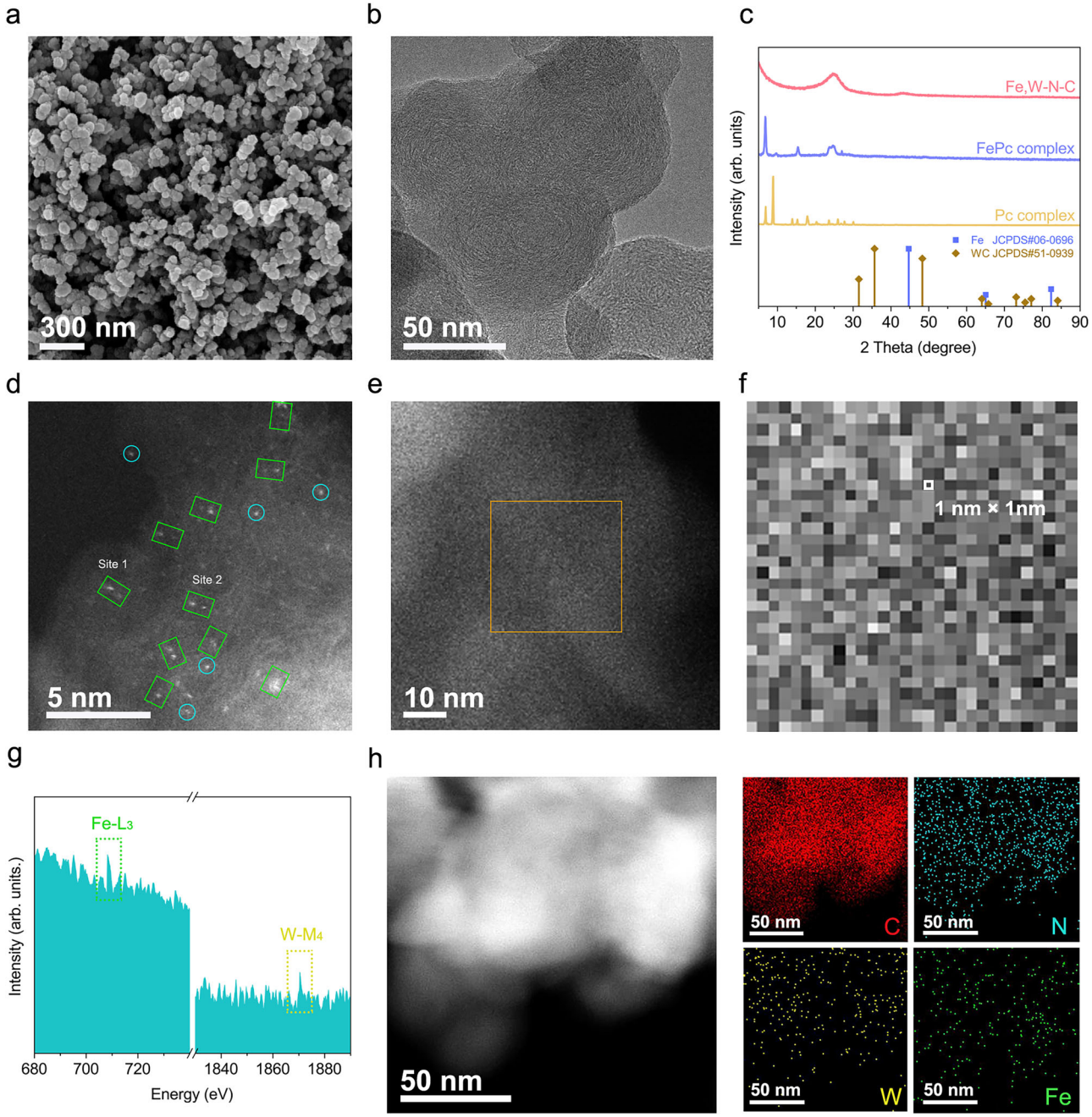

Fig. 2 | Structural characterization of Fe,W-N-C catalyst. a SEM image. **b** TEM image. **c** XRD patterns of Fe,W-N-C catalyst, FePc complex, and Pc complex. **d** Aberration-corrected HAADF-STEM image. **e** HAADF-STEM image and the corresponding STEM-EELS mapping (**f**) taken from the orange boxed area in (**e**). **g** The corresponding EELS spectrum of the 1 nm×1 nm selected small area in (**f**). **h** HAADF-STEM image and the corresponding EDX elemental mapping images for C (red), N (blue), W (yellow), and Fe (green).

pointed out in Fig. 3g is valid. Furthermore, in order to further verify the structure features, the XANES simulations for this representative structure (R = 7 Å cluster) using the FDMNES code were calculated and shown in Fig. 3h, i. It turned out that the theoretically calculated spectra showed similar features to the experimental spectra, particularly for the shape and the position of the peaks, demonstrating the well-defined structure of Fe,W-N-C catalyst.

Electrochemical catalytic properties

The electrochemical ORR performance of the Fe,W-N-C catalyst was assessed using a rotating disk electrode (RDE) in oxygen-saturated 0.1 M KOH electrolytes. To verify the vital role of the Fe-N_4/W-N_4 diatomic sites in oxygen electrocatalysis, Fe,WC-N-C catalyst (with isolated Fe atom and tungsten carbide nanoparticles coexisting) was synthesized using a similar method (Supplementary Figs. 18 and 19). As shown in Fig. 4a, the diatomic Fe,W-N-C catalyst exhibited a notable ORR catalytic activity with the most positive onset potential (1.03 V) and half-wave potential ($E_{1/2}$, 0.90 V) among other synthesized catalysts and the commercial Pt/C catalyst. Specifically, the $E_{1/2}$ of the Fe,W-N-C catalyst is 60 mV and 30 mV higher than that of the single atom Fe-N-C catalyst and the Fe,WC-N-C catalyst, confirming the positive effect of the 5*d*-W species on the single atom 3*d*-Fe catalyst which can be maximized when the 5*d*-W species is also in single atom form. Fe,W-N-C also possessed the highest kinetic current density up to 17.14 mA cm^{-2} at 0.82 V, nearly two times higher than the commercial Pt/C catalyst (Fig. 4b and Supplementary Table 3). Compared with the

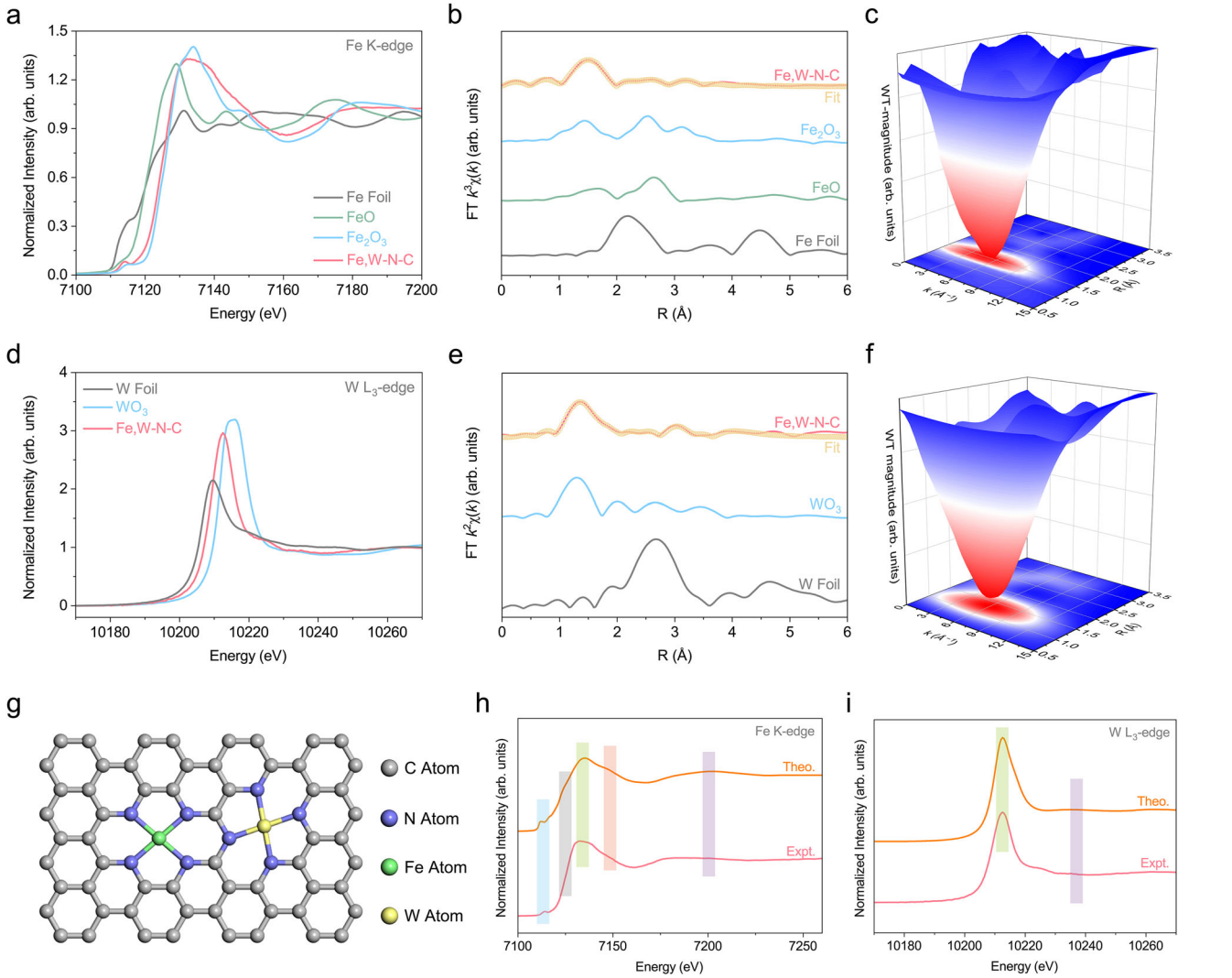

Fig. 3 | X-ray absorption spectroscopy characterization of Fe,W-N-C catalyst. **a** Normalized Fe K-edge X-ray absorption near-edge structure (XANES) spectra of Fe foil, FeO, Fe_2O_3, and Fe,W-N-C catalyst. **b** Fourier transform k^3-weighted Fe K-edge extended X-ray absorption fine structure (FT-EXAFS) spectra at R space and FT-EXAFS fitting curves of Fe,W-N-C. **c** 3D contour wavelet transformed Fe K-edge EXAFS map of the Fe,W-N-C catalyst. **d** Normalized W L_3-edge XANES spectra of W foil, WO_3, and Fe,W-N-C. **e** k^2-weighted W L_3-edge FT-EXAFS spectra and FT-EXAFS fitting curves of Fe,W-N-C. **f** 3D contour wavelet transformed W L_3-edge EXAFS map of the Fe,W-N-C catalyst. **g** The atomic structure model of the Fe,W-N-C catalyst. **h** Comparison between the experimental Fe K-edge XANES spectrum of Fe,W-N-C and the theoretical spectrum calculated for the atomic structure in (**g**). **i** Comparison between the experimental W L_3-edge XANES spectrum of Fe,W-N-C and the theoretical spectrum calculated for the atomic structure in (**g**).

single atom Fe-N-C catalyst, the 3*d*-5*d* hybrid Fe-N_4/W-N_4 diatomic site exhibited a lower Tafel slope (94 mV dec^{-1}), revealing its lower oxygen binding energy and faster ORR kinetics (Supplementary Fig. 20, and Supplementary Table 4)[15,50,51]. The electrochemically active surface areas (ECSAs) of Fe,W-N-C and commercial Pt/C catalysts were estimated and compared by calculating the double-layer capacitance values (Cdl) via cyclic voltammetry curves (Supplementary Fig. 21). The higher Cdl value of the Fe,W-N-C catalyst compared to that of the commercial Pt/C catalyst, indicates its larger ECSA and more approachable active sites. Given its limited BET specific surface area of 75.6 m^2 g^{-1} (Supplementary Fig. 22), it can be concluded that most of the active sites exist on the carbon black surface.

The electron transfer numbers at various potentials were calculated using the linear sweep voltammetry curves collected at different RDE rotating speeds. As shown in Fig. 4c, d, the limiting current density increases with the rotation speed, and the electron transfer numbers were calculated to be ~ 4 in the potential range of 0.2-0.8 V. Also, a nearly complete 4-electrons transfer pathway and less than 2.55 % H_2O_2 yield could be observed in a wide potential range from 0.2 to 1.0 V by rotating ring disk electrode (RRDE) measurements, further certifying the high selective to the 4-electrons transfer pathway (Fig. 4e). This is highly desirable since the competing 2-electrons transfer pathway not only reduces the energy efficiency, but also poisons the Fe active site through the Fenton reaction between the generated H_2O_2 and the Fe sites[52–54]. To confirm the effect of the W-N_4 site in the Fe,W-N-C catalyst after the Fe-N_4 site being poisoned, the nitrite stripping tests were conducted[55]. As shown in Supplementary Fig. 23, the reduced activity after introducing nitrite indicates that the Fe-N_4 site in the Fe, W-N-C catalyst is the adsorption site of O_2/ ORR intermediates. It is worth noting that the ORR catalytic activity did not decrease completely to the metal-free level, indicating that the W-N_4 site can also drive the ORR process at a higher overpotential. After that, the gravimetric site density (MSD) of Fe-N_4 site in Fe,W-N-C catalyst was roughly estimated as at least 10.18 μmol g^{-1} (due to the high hydrogen evolution catalytic activity of the W site at high overpotentials[56,57], which will mask the dissolution peak[55]) by analyzing the current density difference between the unpoisoned and poisoned curves. Since the ORR kinetic current density of the Fe,W-N-C catalyst at 0.95 V (vs RHE) in 0.1 M

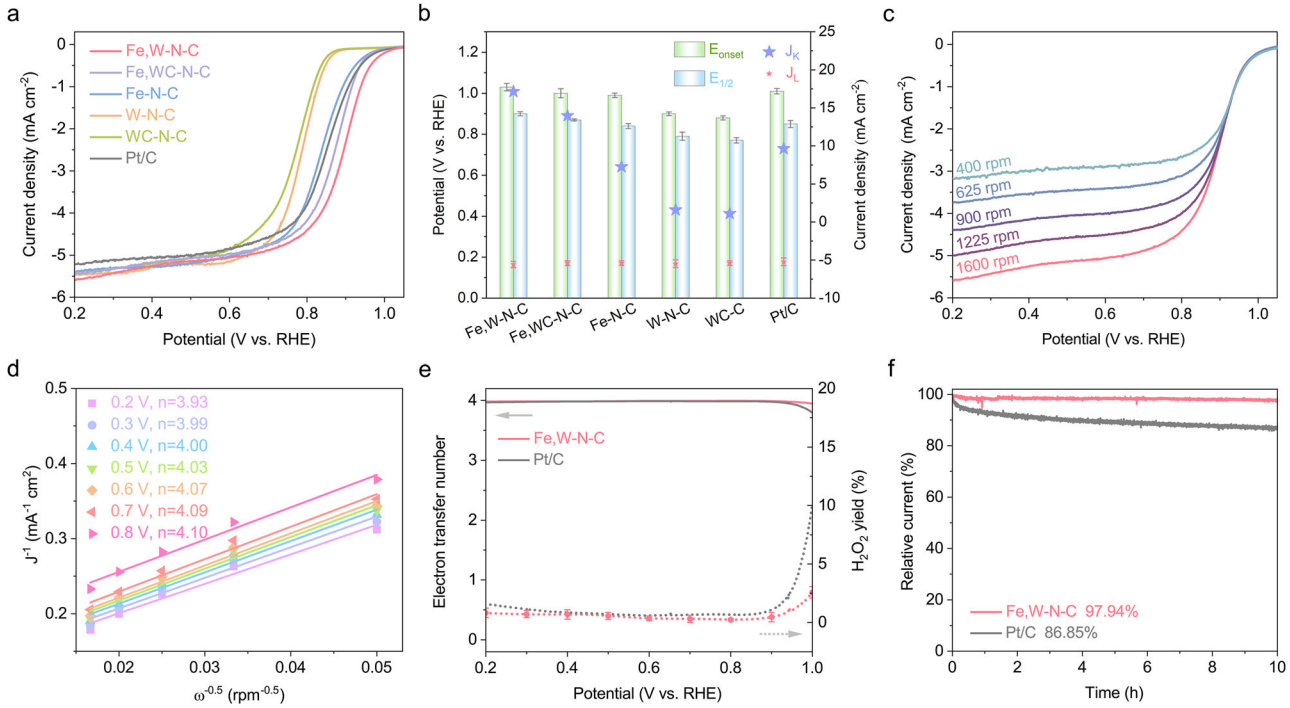

Fig. 4 | Electrocatalytic performance of Fe,W-N-C and other reference catalysts. **a** LSV curves without iR correction for Fe,W-N-C, Fe,WC-N-C, Fe-N-C, W-N-C, WC-N-C, and commercial 20 wt% Pt/C catalysts in oxygen-saturated 0.1 M KOH electrolyte (25 ± 1 °C, pH=13.0 ± 0.5, the resistance of the solution was 45 ± 5 Ω) at 1600 rpm with scan rate of 5 mV s^{-1}. **b** Onset potential (E_{onset}), half-wave potential ($E_{1/2}$) and kinetic current density (J_K) (0.82 V, V versus RHE) for the different catalysts. **c** ORR polarization curves of the Fe,W-N-C catalyst at different rotating speeds. **d** Koutecky-Levich plots and electron transfer numbers at different potentials of the Fe,W-N-C catalyst. **e** H_2O_2 yield and electron transfer number of Fe,W-N-C and Pt/C catalysts measured by RRDE. **f** Chronoamperometric response curves for Fe,W-N-C and Pt/C catalysts.

KOH electrolyte is 0.83 mA cm^{-2}, the turnover frequency (TOF) of the Fe,W-N-C catalyst is estimated to be 4.2 s^{-1}.

Besides catalytic activity and selectivity, methanol tolerance and durability are also essential indices for evaluating the ORR catalytic performance. As displayed in Supplementary Fig. 24, the Fe,W-N-C catalyst exhibited high methanol tolerance ability with negligible current density decay. In contrast, the commercial Pt/C catalyst suffered from a sharp drop in the current. Additionally, the Fe,W-N-C catalyst demonstrated a satisfying ORR long-term catalytic stability with a relative current density retention of 97.94% after a 10-h chronoamperometric test (Fig. 4f). Due to the unique 3*d*-5*d* hybrid Fe-N_4/W-N_4 dual-atom site, the ORR catalytic performance of Fe,W-N-C is comparable to other reported high-activity noble/non-noble metal catalysts (Supplementary Table 5). The stability of Fe,W-N-C catalyst has been further tested by potential cycling from 0.2 V to 1.1 V. As shown in Supplementary Fig. 25, the 1500th CV curve is largely consistent with the initial one, and the LSV curves indicate that despite the catalyst undergoing 1500 cycles of CV tests, there is no obvious decay in $E_{1/2}$ and limited current density, suggesting the outstanding ORR stability of the Fe,W-N-C catalyst. By comparing the CV and ICP results before and after the accelerated durability test (It was found that the Fe content in the catalyst before and after the accelerated durability test were accounted for 1.25 wt% and 1.24 wt%, respectively), negligible metal leaching was observed, which further demonstrated the enhanced catalytic stability of the Fe,W-N-C catalyst.

Inspired by the good ORR catalytic performance, we further examined its catalytic performance in oxygen evolution reaction (OER) to evaluate its potential application as a cathode for rechargeable ZABs. As illustrated in Supplementary Fig. 26 and Supplementary Table 6, the Fe,W-N-C catalyst exhibited the lowest potential as 1.56 V to deliver a current density of 10 mA cm^{-2}, among Fe,WC-N-C (1.68 V), Fe-N-C (1.81 V), W-N-C (1.64 V), WC-N-C(1.72 V), and the benchmark IrO_2 (1.59 V) catalysts. Additionally, the smallest Tafel slope of Fe,W-N-C catalyst confirmed its more favorable OER kinetics (87 mV dec^{-1}, Supplementary Fig. 27). Most importantly, the Fe,W-N-C catalyst also demonstrated high OER catalytic stability for over a 15-h chronopotentiometry test, far exceeding the commercial IrO_2 catalyst (Supplementary Fig. 28).

ZABs performance and in situ characterizations

Given the enhanced ORR and OER catalytic activity and stability, rechargeable ZABs with Fe,W-N-C catalyst loaded on the cathode were assembled to demonstrate their practicability. As shown in Supplementary Figs. 29 and 30, the ZAB with Fe,W-N-C cathode delivered a high specific capacity of 781 mAh g^{-1} and a corresponding energy density up to 953 Wh kg^{-1}, outperforming the ZAB with commercial Pt/C + IrO_2 catalyst (specific capacity: 678 mAh g^{-1}; energy density: 780 Wh kg^{-1}). Notably, the cell exhibited a stable and repeatable discharge/charge cycling curve for over 10,000 h (over 30,000 cycles) at the current density of 5 mA cm^{-2} with negligible decay on the discharge/charge voltage (the voltage gap is nearly unchanged and maintained at around 0.72 V) and areal energy density (based on the area of the air cathode), which is comparable to other reported ZABs (Fig. 5a, Supplementary Figs. 31-33). Even when operated at a high current density of 50 mA cm^{-2}, the Fe,W-N-C based ZAB still can deliver stable performance for over 2000 h (12,000 cycles), far exceeding the ZAB with commercial Pt/C + IrO_2 as the cathode and other reported ZABs (Supplementary Figs. 34 and 35). Surprisingly, the Fe,W-N-C based ZAB exhibited a relatively stable discharge/charge cycling curve of more than 550 h at the current density of 100 mA cm^{-2}, revealing its possibility of stable operation in high-current power-consuming facilities (Supplementary Figs. 36 and 37). Such high ZAB stability has seldom been achieved to date (Supplementary Table 7). In addition, the Fe,W-N-C cathode ZAB presented a high discharged voltage

https://doi.org/10.1038/s41467-025-63540-w

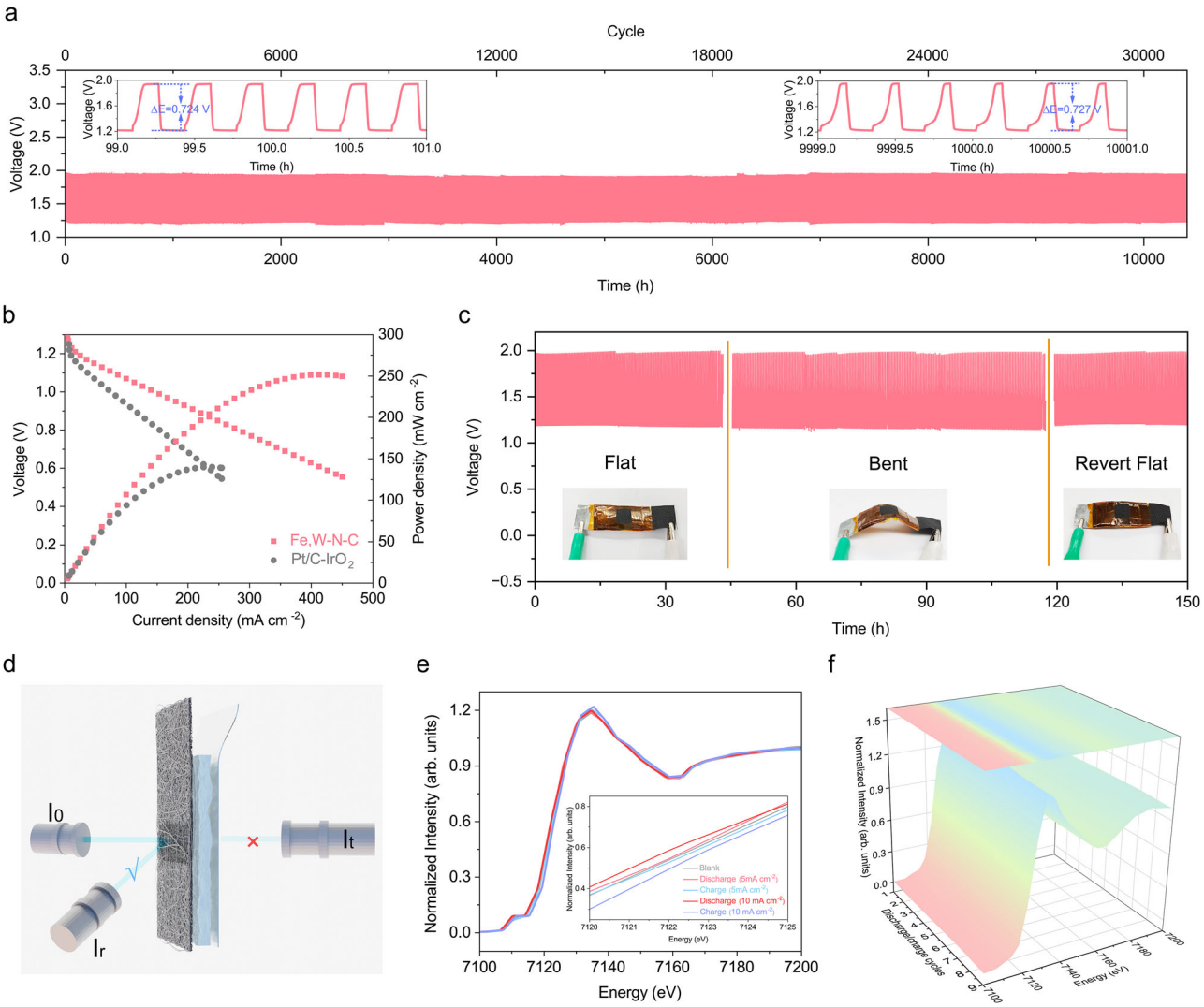

Fig. 5 | Performances of ZABs with Fe,W-N-C air cathode and in situ XAS characterizations. a Galvanostatic discharge/charge cycling stability tests for liquid-state ZAB based on Fe,W-N-C air cathode at a current density of 5 mA cm^{-2}. **b** Discharge polarization and power density plots of Fe,W-N-C and Pt/C-IrO_2 based ZABs. **c** Cycling stability test of the flexible solid-state ZAB with Fe,W-N-C air cathode at a current density of 5 mA cm^{-2}, and the insets are digital photos of the ZAB at flat/bent/revert flat states. **d** Simplified schematic illustration of the solid-state ZAB during the in situ XAS tests. **e** Fe K-edge XANES spectra of Fe,W-N-C based ZAB during the discharging and charging processes at different current densities. **f** Fe K-edge XANES spectra of Fe,W-N-C based ZAB in resting state after several discharge/charge cycles.

plateau with a maximum peak power density of 252 mW cm^{-2}, in contrast to only 140 mW cm^{-2} for the Pt/C + IrO_2 based ZAB (Fig. 5b), demonstrating its practical application potential as an alternative catalyst to Pt-based catalysts in ZABs. To meet the demand for flexible energy devices, we also assembled a flexible solid-state ZAB with Fe,W-N-C as the cathode. As shown in Fig. 5c and Supplementary Figs. 38 and 39, the solid-state ZAB remains stable even after the iterative bending test. It can also light up a series of LED lights on a luminous wristband, promising its practical application in flexible electronics (Supplementary Fig. 40).

To trace the origin of the notable stability, solid-state ZAB with Fe,W-N-C cathode was assembled and in-situ XAS analyses were carried out as illustrated in Fig. 5d. The ZAB was first discharged and charged at 5 mA cm^{-2} and then cycled at a higher current density of 10 mA cm^{-2} after a 2-min rest. As shown in Fig. 5e, the Fe adsorption edge slightly shifts to lower energy compared to the blank state during the first discharge process, and then moves back to higher energy during the charge process. This low-high energy shift repeated in the second discharge/charge cycle, indicating that the discharge/charge processes of ZAB indeed have certain fluctuations in the valence state of the Fe center, which could be attributed to the adsorption of reactants/reaction intermediates on Fe site. The intensity of the pre-edge peak in Fe K-edge XANES is slightly lower than that in ex-situ measurement, suggesting the adsorption of reactants on Fe. Based on the fluctuation of the valance state and the decrease in pre-edge intensity, Fe can be safely identified as the central metal of the active site in both ORR and OER processes. Despite fluctuations in the valence state of Fe during the discharge/charge cycles, the oxidation state remained between +2 and +3 without over-oxidization or over-reduction to cause Fe aggregation or dissolution (Supplementary Fig. 41). Furthermore, nine XANES curves were recorded at the resting state of the ZAB after each discharge/charge cycle, and the oxidation state of the Fe remained stable, which further demonstrates its catalytic stability (Fig. 5f).

Theoretical insights into the activity and stability improvement

The density functional theory (DFT) calculations were conducted to clarify the regulation of 5*d* W-N_4 sites on neighboring Fe-N_4 sites. Based

https://doi.org/10.1038/s41467-025-63540-w

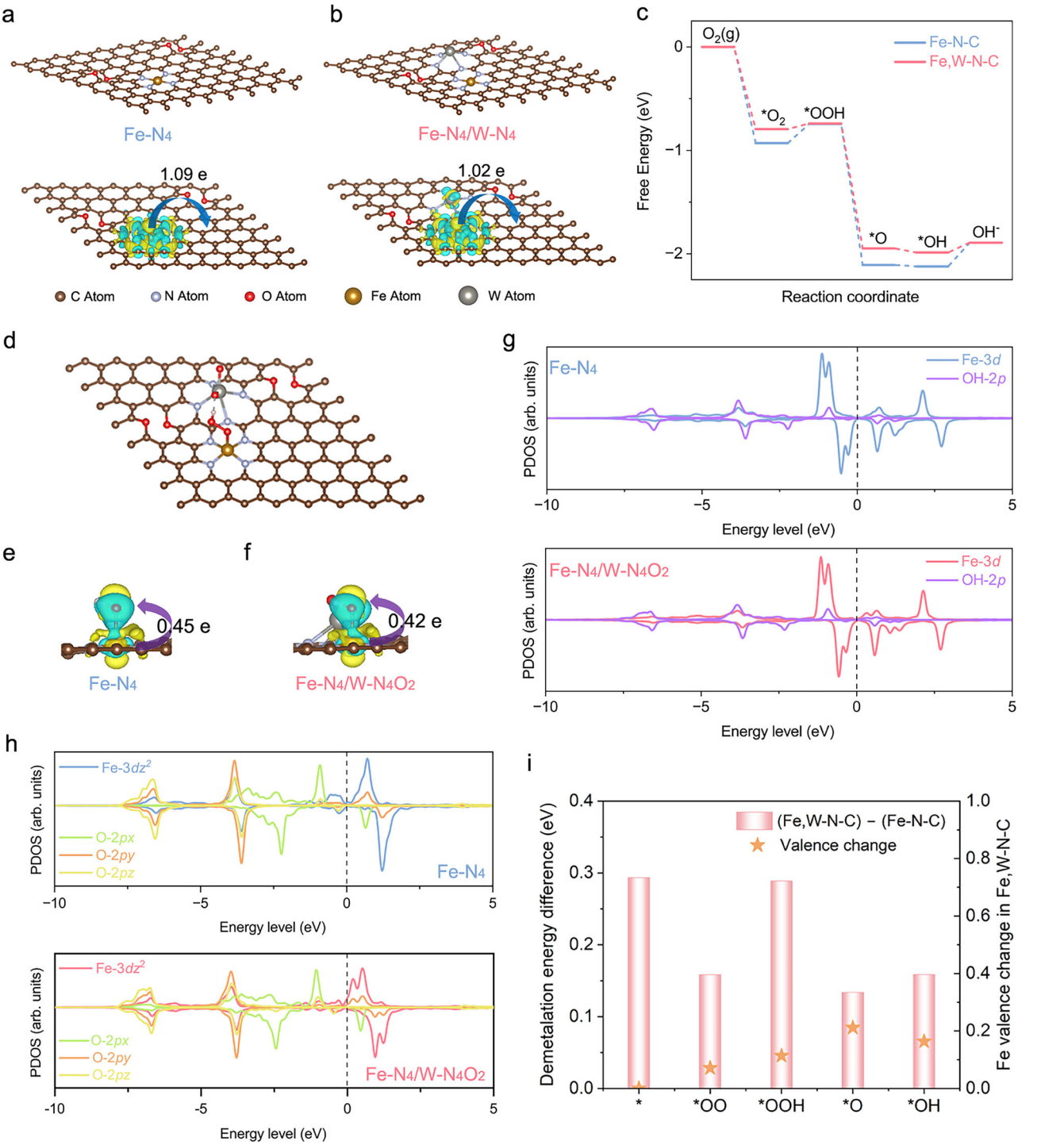

Fig. 6 | Density functional theory calculations for ORR catalysis. Atomic configurations and charge density differences of (**a**) Fe-N_4 and (**b**) Fe-N_4/W-N_4 configurations in Fe-N-C and Fe,W-N-C catalysts, where charge depletion and accumulation were depicted by cyan and yellow, respectively. **c** The free energy diagram of ORR through a $4e^-$ pathway on the active sites of Fe-N-C and Fe,W-N-C catalysts under the electrode potential of 0 V at pH=13. **d** The atomic configuration of *OOH intermediate on Fe-N_4/W-N_4 site, where the dash line represents the generated hydrogen bond between the H atom in *OOH intermediate and the absorbed O atom from the W-N_4O_2 site. The charge density difference and Bader charge transfer diagrams of *OH on (**e**) Fe-N_4 and (**f**) Fe-N_4/W-N_4O_2 sites. **g** Projected density of state (PDOS) analysis of Fe-3*d* orbital with *OH intermediates on Fe-N_4 and Fe-N_4/W-N_4O_2 sites. **h** PDOS analysis of Fe-3dz^2 orbital with O 2*px*/2*py*/2*pz* orbitals in *OH intermediate on Fe-N_4 and Fe-N_4/W-N_4O_2 sites. **i** The valence changes of Fe atoms in Fe,W-N-C catalyst during ORR process and the demetallation energy differences between Fe,W-N-C and Fe-N-C catalysts.

on the HAADF-STEM-EELS, XPS, and XAS analysis, the atomic configurations of the main active sites in Fe-N-C and Fe,W-N-C catalysts are illustrated in Figs. 6a and 6b (Supplementary data 1). By analyzing the charge density differences of the Fe-N_4 and 3*d*-5*d* hybrid Fe-N_4/W-N_4 sites, it could be found that after modification with the neighboring 5*d* W-N_4 site, the electron transfer from Fe atoms to the surrounding decreased, indicating the reduced oxidation state of the Fe atom, consistent with the XAS results. Given the oxygen-rich environment in ORR, we analyzed the adsorption and transition pathways of O_2 on the W-N_4 site. As shown in Supplementary Fig. 42, the adsorption of O_2

molecules on W will spontaneously convert from the end-on adsorption to the side-on adsorption, and the O-O bond will break and form a stable W-$(O)_2$ configuration, which remains the same during the catalytic process. Therefore, the actual active site in Fe,W-N-C catalyst should be denoted as Fe-N_4/W-N_4O_2. To further clarify the regulation of 5*d* W-N_4O_2 sites on Fe-N_4 sites and the effects on ORR catalytic activity, we investigated the ORR catalytic process at pure Fe-N_4 sites and 3*d*-5*d* hybrid Fe-N_4/W-N_4O_2 sites. As illustrated in Fig. 6c, due to the strong adsorption of *OH on the Fe center of the Fe-N-C catalyst, the potential-determining step is the desorption of *OH. Also, the positive ΔG for O_2 activation ($*O_2 \rightarrow *OOH$) step reveals its inertness. In contrast, after introducing the neighboring 5*d* W-N_4O_2 site, the intramolecular hydrogen bond forms between the H atom in *OOH and the O atom in the W-N_4O_2 site, accelerating the activation of O_2 (Fig. 6d). Most importantly, the energy required for the desorption of *OH (rate-determining step) was reduced by 0.14 eV, suggesting that the formation of 3*d*-5*d* hybrid Fe-N_4/W-N_4O_2 is beneficial for optimizing the adsorption energies of ORR intermediates. This maybe due to the electron-withdrawing effect of the adjacent W-N_4O_2 site on Fe site, which leads to a decrease in the electron density of Fe (the positive charge on Fe in the Fe-N-C catalyst and Fe,W-N-C catalyst are 1.085 and 1.103, respectively, Supplementary Fig. 43), thereby affecting the amount of charge that can transferred to *OH, which is beneficial to the desorption of *OH. The Bader charge transfer results revealed that the *OH accepted less charge from Fe-N_4/W-N_4O_2 site than pure Fe-N_4 site, which also confirmed the weak adsorption and stronger desorption ability of *OH on Fe-N_4/W-N_4O_2 site. (Fig. 6e, f). The Projected density of state (PDOS) analysis also corroborated that the introduction of neighboring 5*d* W-N_4O_2 site reduces the overlap between the Fe-3*d* orbitals and O-2*p* orbitals (in *OH intermediates), especially the overlap between Fe-3dz^2 orbital and O-2*pz* and 2*py* orbitals, which leads to the weak adsorption of *OH (Fig. 6g, h, Supplementary Fig. 44 and 45).

As for the OER process, since the initial system is not an oxygen-saturated environment, the active site of Fe,W-N-C catalyst is first assumed to be the original Fe-N_4/W-N_4 site of the catalyst. However, when the W-N_4 site serves as the adsorption site of the H_2O/OER intermediates, the desorption of $*O_2$ from the W-N_4 site requires higher energy, which reveals the inertness of OER on the W-N_4 site in the Fe, W-N-C catalyst (Supplementary Fig. 46). This also proves that in the OER reaction, the W-N_4 site will eventually form the configuration of W-N_4O_2. Also, under the modification of the W-N_4O_2 site, lower energy is required for Fe-N_4 site to drive the OER processes. It is further proved that during the OER reaction, the Fe-N_4 site is also the real adsorption site of the H_2O/OER intermediates, while the W-N_4O_2 site is used to optimize its electronic structure to promote the occurrence of OER.

To reveal the catalytic stability of the Fe-N_4/W-N_4O_2 site, the oxidation state transition of Fe atoms and the demetallation energy of the Fe site during the ORR process were calculated. As shown in Fig. 6i, the oxidation state of Fe atoms tends to be stable in each step under the regulation of the neighboring 5*d* W-N_4O_2 site, indicating that Fe atoms will not be over-oxidized or over-reduced by the adsorbed oxygen-containing intermediates. Notably, the positive demetallation energy differences between the Fe-N_4/W-N_4O_2 and Fe-N_4 sites in all reaction stages demonstrate the strong binding energy of Fe-N bonds in Fe-N_4/W-N_4O_2 site, which well explains the enhanced catalytic stability of the Fe,W-N-C catalyst.

Discussion

This work reports a sustainable and scalable approach to construct highly active Fe-N_4/W-N_4 dual-atomic sites, utilizing 100% of the precursors and generating no byproducts. Under the highly energetic environment of ball milling, we utilized the electron donor-acceptor interactions between Pc and FePc to bring them in close adjacent, and used the N_4 site in Pc to trap the fresh W atoms scratched off from milling balls. This strategy has been successfully adapted to construct other M-N_4/W-N_4 dual-atomic sites by replacing FePc with other metal phthalocyanines. The W atom may even be replaced to fabricate more genetic M_1-N_4/M_2-N_4 sites if specific milling balls containing desired metals are manufactured. In the ORR reaction, the neighboring W-N_4 site facilitates the desorption of *OH on the Fe center and increases the demetallization energy of FeN_4 sites, resulting in a zinc-air battery with a high energy density of 953 Wh kg^{-1} and cycling stability for more than 10,000 h. This low-cost catalyst not only paves the road for the large-scale commercial deployment of zinc-air batteries but also provides a feasible approach for the design of advanced 3*d*-5*d* metal hybrid electrocatalysts.

Methods

Reagents and materials

Carbon black super P (99%, Thermo Fisher Scientific Chemicals), phthalocyanine crystalline (Pc, 98%, Thermo Fisher Scientific Chemicals), iron (II) phthalocyanine (FePc, 96%, Thermo Fisher Scientific Chemicals), cobalt (II) phthalocyanine (CoPc, 93%, Tokyo Chemical Industry Co. Ltd), nickel phthalocyanine (NiPc, 95%, Thermo Fisher Scientific Chemicals), Nafion dispersion D520 (Fuel Cell Store), 2-propanol (C_3H_8O, 99.5%, Fisher Chemical), methanol (CH_3OH, 99.8%, Fisher Chemical), potassium hydroxide (KOH, 90%, Sigma-Aldrich), zinc acetate dihydrate (98%, Thermo Fisher Scientific Chemicals), iridium (IV) oxide (IrO_2, Premion 99.99%, Alfa Aesar), 20% platinum on carbon (Fuel Cell Etc.) were used as received. The 18.2 MΩ-cm ultrapure water was obtained from the Mili-Q system.

Synthesis of catalysts

In a typical synthesis of dual-atom Fe,W catalyst, an appropriate amount of tungsten carbide grinding balls were put into the tungsten chamber of a planetary ball mill equipment. Then, 500 mg carbon black powder, 200 mg phthalocyanine crystalline and 101.5 mg iron (II) phthalocyanine complex were added. The mixture was ground for 15 cycles at room temperature with a rotation speed of 150 rpm, a 5 min stop was set to change the direction of rotation during the 5 min clockwise and 5 min counter-clockwise cycle. The precursor mixture was then annealed at 900 °C for 2 h under a gas flow of 100 sccm Ar. After cooling down to room temperature, the dual-atom Fe,W catalyst was obtained and named as Fe,W-N-C.

Other dual-atom catalysts, i.e., Co,W-N-C and Ni,W-N-C were prepared by using the same synthesis procedures with different phthalocyanine-metal complexes (cobalt (II) phthalocyanine for Co,W-N-C and nickel phthalocyanine for Ni,W-N-C) instead of iron (II) phthalocyanine complex.

Fe single atom-tungsten carbide nanoparticle coexistence catalyst (Fe,WC-N-C) and W single atom catalyst (W-N-C) were synthesized by using a similar method to Fe,W-N-C catalyst, except for without the addition of phthalocyanine crystalline and iron (II) phthalocyanine complex in the ball milling step, respectively. Similarly, tungsten carbide nanoparticle catalyst (WC-C) was prepared by using the same method with Fe,W-N-C catalyst, except for without the addition of both phthalocyanine crystalline and iron (II) phthalocyanine complex. As a comparison, Fe single atom catalyst (Fe-N-C) was also synthesized by using the same method with Fe,W-N-C catalyst, except that agate grinding balls were used instead of tungsten carbide grinding balls to avoid introducing tungsten into the Fe-N-C catalyst.

Characterization methods

The morphology and detailed structure of catalysts were investigated by using field-emission scanning electron microscopy (Hitachi S-4800) and transmission electron microscopy (JEOL JEM-ARM200CF S/TEM) equipped with energy-dispersive X-ray spectroscopy (EDX) and

electron energy loss spectroscopy (EELS). The phase composition was revealed by X-ray diffraction pattern with Bruker D8 Discover diffraction system. X-ray photoelectron spectroscopy experiments were performed by using Kratos Axis (Ultra) spectrometer with monochromatized Al Kα (hυ = 1486.71 eV). The spectrometer was calibrated by the binding energy (84.0 eV) of Au $4f_{7/2}$ with reference to the Fermi level. Charge effects were corrected by using C 1 s peak at 284.8 eV. The inductively coupled plasma-optical emission spectroscopy (iCAP 6300) was used to detect the metal content in different samples. The synchrotron X-ray absorption spectra of Fe and W were recorded on the hard X-ray microanalysis beamline (HXMA-061D) of Canadian Light Source. XANES data analysis, EXAFS fitting and wavelet transformation were performed with Athena, Artemis and HAMA Fortran version software packages, respectively[58–60]. All spectra were collected in ambient conditions.

Electrochemical measurements

The catalyst inks were prepared by dispersing 2 mg catalyst in a mixture of 400 μL isopropanol/ultrapure water/5 wt % Nafion solution (190 μL/190 μL/20 μL). The obtained mixture was ultrasonicated for 120 min before use. Subsequently, 8 μL of the suspension was dropped by a pipettor onto the surface of a polished glassy carbon rotating disk electrode (RDE, 0.19625 cm^{-2}) or rotating ring-disk electrode (RRDE) and naturally dried in air. The working electrode for the oxygen reduction reaction (ORR) electrochemical test was catalyst-loaded RDE/RRDE with a catalyst loading of 0.2 mg cm^{-2}. As for the oxygen evolution reaction (OER), a carbon paper electrode (1 cm^{-2}) coated with 0.2 mg cm^{-2} catalyst was used as the working electrode.

All of the ORR and OER electrochemical measurements were carried out in a conventional three-electrode system by a Bio-Logic electrochemical workstation equipped with a pine modulated speed rotator. The catalyst modified electrode, a graphite rod and Ag/AgCl electrode (3.5 M KCl) were employed as the working electrode, counter electrode, and reference electrode, respectively. All obtained potentials were converted to the reverse hydrogen electrode (RHE) potentials according to Nernst Eq. (1) and without iR-compensation:

$$E_{RHE} = E_{Ag/AgCl} + 0.0591 \times pH + 0.205 \quad (1)$$

The ORR linear sweep voltammetry (LSV) polarization curves were conducted in O_2-saturated freshly-prepared 0.1 M KOH electrolyte (pH=13.0 ± 0.5, the resistance of the solution was 45 ± 5 Ω) and recorded at different rotation speeds from 400 to 2500 rpm with a scan rate of 5 mV s^{-1}. The electron transfer number (n) was calculated based on Koutecky-Levich Eqs. (2)-(4):

$$\frac{1}{J} = \frac{1}{J_L} + \frac{1}{J_K} = \frac{1}{B\omega^{1/2}} + \frac{1}{J_K} \quad (2)$$

$$B = 0.62nFC_O D_O^{2/3} V^{-1/6} \quad (3)$$

$$J_K = nFkC_O \quad (4)$$

where J is the measured current density (mA cm^{-2}), J_L is the diffusion limiting current density (mA cm^{-2}), J_K is the kinetic current density (mA cm^{-2}), ω is the angular velocity of the disk, n is the electron transfer number, F is the Faraday constant (96485 C mol^{-1}), C_O is the saturated O_2 concentration (1.2×10^{-6} mol cm^{-3}), D_O is the diffusion coefficient of O_2 in the electrolyte (1.9×10^{-5} cm^2 s^{-1}), and V is the kinematic viscosity (0.01 cm^2 s^{-1}).

The number of electron transfer and the yield of hydrogen peroxide on RRDE were calculated on the basis of the currents of the disk electrode and ring electrode by using the following Eqs. (5)-(6):

$$n = \frac{4I_d}{I_d + (\frac{I_r}{N})} \quad (5)$$

$$\%H_2O_2 = \frac{200I_r/N}{I_d + (\frac{I_r}{N})} \quad (6)$$

where I_d is the disk current, I_r is the ring current, N is the H_2O_2 collection efficiency of the ring.

The double-layer capacitance values (Cdl) was analysis by recording the cyclic voltammetry curves between 1.06 V-1.16 V with different scan rates of 10 mV s^{-1} to 100 mV s^{-1}. The ORR stability tests were performed by measuring the current change at an operation potential of 0.8 V (vs. RHE) for 10 h.

For OER electrochemical measurements, freshly-prepared 1.0 M KOH electrolyte was used as the electrolyte (the resistance of the solution was 1.7 ± 0.2 Ω), and the long-term stability test was completed by chronopotentiometry at a constant current density of 10 mA cm^{-2}.

Determining active site density via the nitrite stripping method

Cleaning protocol. To obtain a non-changing oxygen reduction performance and cyclic voltammograms (CV) for the duration of the experiment, extensive cycling (20 cycles in Ar-saturated electrolyte at 100 mV s^{-1}, 10 cycles in Ar-saturated electrolyte at 10 mV s^{-1}, and 6 cycles in O_2-saturated electrolyte at 5 mV s^{-1} with the potential range of 1.05 to -0.4 V) were repeated performed to make the layer hydrophilic and allow a complete wetting. All experiments for active site density determination were performed in a 0.5 M acetate buffer at pH=5.2 with a catalyst loading amount of 0.27 mg cm^{-2}.

Measurement (unpoisoned). a. The LSV curve was recorded in O_2-saturated electrolyte within the voltage range from 1.0 V to 0.3 V with a scan rate of 5 mV s^{-1}. b. The CV curve was recorded in Ar-saturated electrolyte within the voltage range of 0.45 V to -0.15 V with a scan rate of 10 mV s^{-1}.

Electrode poisoning. a. The working electrode was dipped in 0.125 M $NaNO_2$ solution for 300 s at open circuit potential (OCP) with a rotation rate of 300 rpm. b. The working electrode was washed in deionized water for 60 s, electrolyte for 300 s, and deionized water for 60 s with a rotation rate of 300 rpm at OCP.

Measurement (poisoned). a. The LSV curve in O_2-saturated electrolyte within the voltage range from 1.0 V to 0.3 V with a scan rate of 5 mV s^{-1} was recorded again. b. The CV curve was also recorded in Ar-saturated electrolyte within the voltage range of 0.45 V to -0.15 V with a scan rate of 10 mV s^{-1}.

The gravimetric site density (MSD) can be calculated by the following Eq. (7):

$$\mathrm{MSD}\,[\mathrm{mole\ sites}\,g^{-1}] = \frac{Q_{strip}[C\,g^{-1}]}{n_{strip}F[C\,mol^{-1}]} \quad (7)$$

The turnover frequency (TOF) at 0.95 V in 0.1 M KOH electrolyte can be calculated via the following Eq. (8):

$$\mathrm{TOF}\,[s^{-1}] = \frac{J_K[A\,g^{-1}]}{F\left[A\,s\,mol^{-1}\right] \times MSD[mol\,g^{-1}]} \quad (8)$$

Where Q_{strip} is the excess coulometric charge associated with the stripping peak, n_{strip} is the number of electrons associated with the reduction of one adsorbed nitrosyl per site and its value is 5, F is the

Faraday constant (96500 C mol^{-1}), J_K is the kinetic current density of the catalyst at 0.95 V in 0.1 M KOH electrolyte.

Assembly and electrochemical measurements of rechargeable ZABs

The performance of the rechargeable liquid-state ZABs was evaluated by the Bio-Logic electrochemical workstation and LAND testing system in a homemade air cell at a temperature of 25 ± 1 °C (relative humidity 45-65%), which consisted of an air cathode (Fe,W-N-C catalyst coated carbon paper, 0.5 mg cm^{-2}), a polished zinc plate anode (1 cm × 3 cm), and electrolyte (6.0 M KOH with 0.2 M zinc acetate). For comparison, the commercial Pt/C and IrO_2 catalysts (mass ratio of 1:1) were also loaded on carbon paper with a loading amount of 1.0 mg cm^{-2} and used as the air electrode of the ZABs. The specific capacity and energy density were determined by the galvanostatic discharge at a current density of 10 mA cm^{-2} and normalized by the mass of consumed Zn foil, as Eq. (9).

$$\text{specific capacity} = \frac{I_{discharge} \times t}{m_{Zn1} - m_{Zn2}} \tag{9}$$

where, $I_{discharge}$ is the discharge current density (10 mA cm^{-2}), t is the time when the reaction stops, m_{Zn1} and m_{Zn2} are the weights of the Zn foil before and after the discharge process, respectively.

The discharge and charge cycling durability of the batteries were evaluated at constant current densities of 5 mA cm^{-2} (catalyst loading: 0.5 mg cm^{-2}), 50 mA cm^{-2} and 100 mA cm^{-2} (catalyst loading: 1.0 mg cm^{-2}).

The rechargeable flexible solid-state ZAB was assembled with a catalyst-coated carbon cloth as the cathode, a polished zinc plate as the anode, and a PVA-KOH-$Zn(CH_3COO)_2$ hydrogel as the solid-state electrolyte. The discharge and charge cycling durability of the battery was evaluated at a constant current density of 5 mA cm^{-2} with LAND battery testing system.

In situ X-ray absorption spectra measurements for flexible solid-state ZABs

The operando XAS spectra of flexible solid-state ZABs were recorded in fluorescence mode. In order to ensure that the Fe element in the cathode of flexible solid-state ZABs could be clearly detected, 200 μL Fe,W-N-C catalyst ink was dropped on the gas diffusion layer and served as the air cathode. The Zn mesh was used as the anode and the glass fiber membrane impregnated with KOH-$Zn(CH_3COO)_2$ electrolyte was served as the solid electrolyte. To obtain the evolution information of the active site in the working state of ZAB, discharge and charge cycle tests were conducted at the current densities of 5 mA cm^{-2} and 10 mA cm^{-2}. During the XAS spectrum collection process, the X-ray absorption edge position was calibrated using standard Fe foil.

Density functional theory (DFT) calculations

All DFT calculations were performed by using the Vienna Ab initio Simulation Package (VASP)[61]. The projector augmented wave (PAW) method was adopted to describe the electron-ion interaction[62]. The Perdew-Burke-Ernzerhof (PBE) exchange-correlation functional within a generalized gradient approximation (GGA) was employed to describe the electron-electron interaction, and a cut-off energy for the plane-wave was set as 450 eV[63]. Moreover, the semiempirical DFT-D3 dispersion correction was applied to describe the weak interactions, including Van der Waals interactions in molecule adsorption and hydrogen bonding[64]. A Γ-centered 2×2×1 k-point mesh was selected to sample the Brillouin zone of hexagonal cells. The convergence criteria for the energy and force were set to 10^{-6} eV and 0.01 eV $Å^{-1}$, respectively. To avoid the interactions between two neighboring images, the vacuum layer thickness was set to be 20 Å. All of the atoms were fully relaxed during the structural optimizations.

The considered reaction steps for the $4e^-$ electrochemical ORR processes under base conditions are generally reported as following Eqs. (10)-(14):

$$O_2\,(g) + * \rightarrow *O_2 \tag{10}$$

$$*O_2 + H_2O\,(l) + e^- \rightarrow *OOH + OH^- \tag{11}$$

$$*OOH + e^- \rightarrow *O + OH^- \tag{12}$$

$$*O + H_2O\,(l) + e^- \rightarrow *OH + OH^- \tag{13}$$

$$*OH + e^- \rightarrow * + OH^- \tag{14}$$

where * represents the catalytic active sites of vacant surface or the intermediate species adsorbed on the active sites. The Gibbs free energy of ORR can be calculated with the following Eq. (15)[13]:

$$\Delta G = \Delta E + \Delta ZPE - T\Delta S + neU + \Delta G_{pH} \tag{15}$$

where ΔE represents the adsorption energy difference for each species adsorbed on the catalyst calculated by VASP, the ΔZPE and ΔS are the zero-point energy and entropy difference between the adsorbed state and corresponding free-standing state, respectively. neU and ΔG_{pH} are the free energy contributions related to the electrode potential U and pH value, respectively. pH value was set as 13 to describe an alkaline media, and the effect of pH on the ΔG was obtained by the following Eq. (16):

$$\Delta G_{pH} = kT \times pH \times \ln 10 \tag{16}$$

The nudged elastic band (NEB) climbing image NEB (CI-NEB) methods were used to estimate the diffusion barrier[65]. All of the atomic geometries were visualized by the program Visualization for Electronic and Structural Analysis (VESTA), including the structures of catalysts and adsorbates, as well as plots of charge density difference[66].

Data availability

All data needed to evaluate the conclusions in the paper are present in the paper and/or the Supplementary Information. Source data are provided with this paper.

References

1. Sun, K. et al. $Co(CN)_3$ catalysts with well-defined coordination structure for the oxygen reduction reaction. *Nat. Catal.* **6**, 1164–1173 (2023).
2. Liu, M. et al. In situ modulating coordination fields of single-atom cobalt catalyst for enhanced oxygen reduction reaction. *Nat. Commun.* **15**, 1675 (2024).
3. Liu, E. & Higgins, D. Tunable layered Mn oxides for oxygen electrocatalysis. *Nat. Catal.* **7**, 469–471 (2024).
4. Gao, R. et al. Pt/Fe_2O_3 with Pt-Fe pair sites as a catalyst for oxygen reduction with ultralow Pt loading. *Nat. Energy* **6**, 614–623 (2021).
5. Jin, X. et al. A highly efficient Fe-N-C electrocatalyst with atomically dispersed FeN_4 sites for the oxygen reduction reaction. *ChemCatChem* **13**, 2683–2690 (2021).
6. Jasinski, R. A new fuel cell cathode catalyst. *Nature* **201**, 1212–1213 (1964).
7. Proietti, E. et al. Iron-based cathode catalyst with enhanced power density in polymer electrolyte membrane fuel cells. *Nat. Commun.* **2**, 416 (2011).

8. Schäfer, F. P. et al. *Phys. Chem. Appl. Dyest.* **61**, 133–181 (1976).
9. Chen, K. et al. Iron phthalocyanine with coordination induced electronic localization to boost oxygen reduction reaction. *Nat. Commun.* **11**, 4173 (2020).
10. Loyola, C. Z. & Tasca, F. Molecular and pyrolyzed penta-coordinated catalysts for the oxygen reduction reaction: a short opinion review on electronic properties and catalytic activity. *Curr. Opin. Electroche.* **40**, 101316 (2023).
11. Serov, A., Artyushkova, K., Andersen, N. I., Stariha, S. & Atanassov, P. Original mechanochemical synthesis of non-platinum group metals oxygen reduction reaction catalysts assisted by sacrificial support method. *Electrochim. Acta* **179**, 154–160 (2015).
12. Wan, X. et al. Iron atom-cluster interactions increase activity and improve durability in Fe-N-C fuel cells. *Nat. Commun.* **13**, 2963 (2022).
13. Tian, H. et al. High durability of Fe-N-C single-atom catalysts with carbon vacancies toward the oxygen reduction reaction in alkaline media. *Adv. Mater.* **35**, 2210714 (2023).
14. Loyola, C. Z., Gatica, A., Troncoso, N., Orellana, W. & Tasca, F. On the effects of Br^-, ClO_4^-, NO_3^- anions on the oxygen reduction reaction electrocatalysis at Fe phthalocyanine modified electrodes. *Electrochim. Acta* **473**, 143416 (2024).
15. Orellana, W. et al. Effect of electrolyte media on the catalysis of Fe Phthalocyanine toward the oxygen reduction reaction: ab initio molecular dynamics simulations and experimental analyses. *ACS Catal.* **12**, 12786–12799 (2022).
16. Zúñiga Loyola, C., Troncoso, N., Gatica Caro, A. & Tasca, F. Electrochemical evaluation of penta-coordinated Fe phthalocyanine during the oxygen reduction reaction in various acidic solutions. *ChemElectroChem* **11**, e202400186 (2024).
17. Zamora Zeledón, J. A. et al. Probing the effects of acid electrolyte anions on electrocatalyst activity and selectivity for the oxygen reduction reaction. *ChemElectroChem* **8**, 2467–2478 (2021).
18. Qin, J. et al. Altering ligand fields in single-atom sites through second-shell anion modulation boosts the oxygen reduction reaction. *J. Am. Chem. Soc.* **144**, 2197–2207 (2022).
19. Ku, Y. P. et al. Oxygen reduction reaction in alkaline media causes iron leaching from Fe-N-C electrocatalysts. *J. Am. Chem. Soc.* **144**, 9753–9763 (2022).
20. Yang, N. et al. Theoretically probing the possible degradation mechanisms of an FeNC catalyst during the oxygen reduction reaction. *Chem. Sci.* **12**, 12476–12484 (2021).
21. Collman, J. P. et al. A cytochrome c oxidase model catalyzes oxygen to water reduction under rate-limiting electron flux. *Science* **315**, 1565–1568 (2007).
22. Hu, C. et al. Inhibiting demetalation of Fe-N-C via Mn sites for efficient oxygen reduction reaction in zinc-air batteries. *Adv. Mater.* **36**, 2405763 (2024).
23. Tang, B. et al. A Janus dual-atom catalyst for electrocatalytic oxygen reduction and evolution. *Nat. Synth.* **3**, 878–890 (2024).
24. Pei, Z. et al. Atomically dispersed Fe sites regulated by adjacent single Co atoms anchored on N-P co-doped carbon structures for highly efficient oxygen reduction reaction. *Adv. Mater.* **36**, 2306047 (2024).
25. He, T. et al. Theory-guided regulation of FeN_4 spin state by neighboring Cu atoms for enhanced oxygen reduction electrocatalysis in flexible metal-air batteries. *Angew. Chem. Int. Ed.* **134**, e202201007 (2022).
26. Zhu, Z. et al. Coexisting single-atomic Fe and Ni sites on hierarchically ordered porous carbon as a highly efficient ORR electrocatalyst. *Adv. Mater.* **32**, 2004670 (2020).
27. Sun, Z. et al. Understanding synergistic catalysis on Cu-Se dual atom sites via operando X-ray absorption spectroscopy in oxygen reduction reaction. *Angew. Chem. Int. Ed.* **62**, e202217719 (2023).
28. Wang, L. et al. The 3d-5d orbital repulsion of transition metals in oxyhydroxide catalysts facilitates water oxidation. *J. Mater. Chem. A* **7**, 14455–14461 (2019).
29. He, R. et al. A 3d-4d-5d high entropy alloy as a bifunctional oxygen catalyst for robust aqueous zinc-air batteries. *Adv. Mater.* **35**, 2303719 (2023).
30. Kim, B. J. et al. Missing *xy*-band fermi surface in 4d transition-metal oxide Sr_2RhO_4: effect of the octahedra rotation on the electronic structure. *Phys. Rev. Lett.* **97**, 106401 (2006).
31. Xin, X. et al. Large electronegativity differences between adjacent atomic sites activate and stabilize $ZnIn_2S_4$ for efficient photocatalytic overall water splitting. *Nat. Commun.* **15**, 337 (2024).
32. Bisen, O. Y., Yadav, A. K. & Nanda, K. K. Self-organized single-atom tungsten supported on the N-doped carbon matrix for durable oxygen reduction. *ACS Appl. Mater. Interfaces* **12**, 43586–43595 (2020).
33. Ma, Y. et al. Localizing tungsten single atoms around tungsten nitride nanoparticles for efficient oxygen reduction electrocatalysis in metal-air batteries. *Adv. Sci.* **9**, 2105192 (2022).
34. Chen, Z. et al. Coordination-controlled single-atom tungsten as a non-3d-metal oxygen reduction reaction electrocatalyst with ultrahigh mass activity. *Nano Energy* **60**, 394–403 (2019).
35. Yuan, R. et al. Structural transformation of porous and disordered carbon during ball-milling. *Chem. Eng. J.* **454**, 140418 (2023).
36. Chen, C. et al. Engineering molecular heterostructured catalyst for oxygen reduction reaction. *J. Am. Chem. Soc.* **145**, 21273–21283 (2023).
37. de la Escosura, A. et al. Donor-acceptor phthalocyanine nanoaggregates. *J. Am. Chem. Soc.* **125**, 12300–12308 (2003).
38. Figueiredo, J. L., Pereira, M. F. R., Freitas, M. M. A. & Orfao, J. J. M. Modification of the surface chemistry of activated carbons. *Carbon* **37**, 1379–1389 (1999).
39. Li, J. et al. Thermally driven structure and performance evolution of atomically dispersed FeN_4 sites for oxygen reduction. *Angew. Chem. Int. Ed.* **58**, 18971–18980 (2019).
40. Zhang, P. et al. Inter-site structural heterogeneity induction of single atom Fe catalysts for robust oxygen reduction. *Nat. Commun.* **15**, 2062 (2024).
41. Murphy, E. et al. Synergizing Fe_2O_3 nanoparticles on single atom Fe-N-C for nitrate reduction to ammonia at industrial current densities. *Adv. Mater.* **36**, 2401133 (2024).
42. Liu, X. et al. Observation of ultrathin Sc-containing surface layer on life-tested scandate cathodes. *IEEE Trans. Electron Devices* **70**, 2876–2882 (2023).
43. Li, Y. et al. Dual-atom Ag_2/graphene catalyst for efficient electroreduction of CO_2 to CO. *Appl. Catal. B* **268**, 118747 (2020).
44. Xing, G. et al. Strengthening oxygen reduction activity based on the cooperation of pyridinic-N and graphitic-N for atomically dispersed Fe sites. *J. Mater. Chem. A* **11**, 9493–9503 (2023).
45. Han, Z. et al. Boosting oxygen reduction of single atomic iron sites by charge redistribution. *Appl. Catal. B* **337**, 122961 (2023).
46. Zang, Y. et al. A pyrolysis-free Ni/Fe bimetallic electrocatalyst for overall water splitting. *Nat. Commun.* **14**, 1792 (2023).
47. Li, J. et al. Identification of durable and non-durable FeNx sites in Fe-N-C materials for proton exchange membrane fuel cells. *Nat. Catal.* **4**, 10–19 (2021).
48. Loyola, C. Z. et al. High content Fe (III) electrocatalyst for the oxygen reduction and evolution reactions. Spectroscopic, electrochemical, and theoretical insights. *Int. J. Hydrog. Energ.* **101**, 605–616 (2025).
49. Chen, S. et al. Dehydrogenation of ammonia borane by platinum-nickel dimers: regulation of heteroatom interspace boosts bifunctional synergetic catalysis. *Angew. Chem. Int. Ed.* **61**, e202211919 (2022).
50. Zhang, H. et al. Tailoring oxygen reduction reaction kinetics of Fe-N-C catalyst via spin manipulation for efficient zinc-air batteries. *Adv. Mater.* **36**, 2400523 (2024).
51. Fletcher, S. Tafel slopes from first principles. *J. Solid State Electrochem.* **13**, 537–549 (2009).

52. Ni, B. et al. Second-shell N dopants regulate acidic O_2 reduction pathways on isolated Pt sites. *J. Am. Chem. Soc.* **146**, 11181–11192 (2024).
53. Li, Y. et al. Main-group element-boosted oxygen electrocatalysis of Cu-N-C sites for zinc-air battery with cycling over 5000 h. *Nat. Commun.* **15**, 8365 (2024).
54. Zhang, P. et al. Generation pathway of hydroxyl radical in Fe/N/C-based oxygen reduction electrocatalysts under acidic media. *J. Phys. Chem. Lett.* **12**, 7797–7803 (2021).
55. Malko, D., Kucernak, A. & Lopes, T. In situ electrochemical quantification of active sites in Fe-N/C non-precious metal catalysts. *Nat. Commun.* **7**, 13285 (2016).
56. Chen, W. et al. Single tungsten atoms supported on MOF-derived N-doped carbon for robust electrochemical hydrogen evolution. *Adv. Mater.* **30**, 1800396 (2018).
57. Yang, Y. et al. O-coordinated W-Mo dual-atom catalyst for pH-universal electrocatalytic hydrogen evolution. *Sci. Adv.* **6**, eaba6586 (2020).
58. Ravel, B. & Newville, M. ATHENA, ARTEMIS, HEPHAESTUS: data analysis for X-ray absorption spectroscopy using IFEFFIT. *J. Synchrotron radiat.* **12**, 537–541 (2005).
59. Funke, H., Scheinost, A. C. & Chukalina, M. Wavelet analysis of extended x-ray absorption fine structure data. *Phys. Rev. B Condens. Matter Mater. Phys.* **71**, 094110 (2005).
60. Funke, H., Chukalina, M. & Scheinost, A. C. A new FEFF-based wavelet for EXAFS data analysis. *J. Synchrotron radiat.* **14**, 426–432 (2007).
61. Kresse, G. & Furthmüller, J. Efficient iterative schemes for ab initio total-energy calculations using a plane-wave basis set. *Phys. Rev. B* **54**, 11169–11186 (1996).
62. Blöchl, P. E. Projector augmented-wave method. *Phys. Rev. B* **50**, 17953 (1994).
63. Perdew, J. P., Burke, K. & Ernzerhof, M. Generalized gradient approximation made simple. *Phys. Rev. Lett.* **77**, 3865 (1996).
64. Grimme, S., Antony, J., Ehrlich, S. & Krieg, H. A. consistent and accurate ab initio parametrization of density functional dispersion correction (DFT-D) for the 94 elements H-Pu. *J. Chem. Phys.* **132**, 154104 (2010).
65. Henkelman, G., Uberuaga, B. P. & Jónsson, H. A climbing image nudged elastic band method for finding saddle points and minimum energy paths. *J. Chem. Phys.* **113**, 9901–9904 (2000).
66. Momma, K. & Izumi, F. VESTA: a three-dimensional visualization system for electronic and structural analysis. *J. Appl. Crystallogr.* **41**, 653–658 (2008).

Acknowledgements

This work was supported by NSERC Alliance (ALLRP 571058-21)-Alberta Innovates Advance program (212200888 (Z. L.)), China Scholarship Council (CSC (Y. L.)), JSPS Kakenhi (24KF0109 (Y. Y.)). We also greatly appreciate Manabu Fujii for the help.

Author contributions

Y.L., H.Z., and Z.L. conceived and designed the project. Y.L. carried out the sample synthesis, characterizations, electrochemical measurements, battery tests and manuscript writing. H.W. carried out the computational investigation and provided the analyses. C.C. contributed to the ICP, STEM-EELS characterization and battery performance analysis. X.X. and Y.Y. assisted with the XAS tests. X.T. and K.J. helped to discuss the experimental data. N.C. contributed to the XAS tests and XANES analysis. Z.L. and H.Z. are responsible for the overall supervision of the project. All the authors participated in preparing the manuscript and contributed to the discussion.

Competing interests

The authors declare no competing interests.

Additional information

Supplementary information The online version contains supplementary material available at https://doi.org/10.1038/s41467-025-63540-w.

Correspondence and requests for materials should be addressed to Hao Zhang or Zhi Li.

Peer review information *Nature Communications* thanks Mohsin Muhyuddin, Mai Thanh Nguyen and the other anonymous reviewer(s) for their contribution to the peer review of this work. A peer review file is available.